

A comparison of energy absorption in axial crush tests between wood veneers, basalt fibre reinforced polymers and hybrid combinations

Johannes Reiner^{*} , Mahbube Subhani , Matt Jennings

School of Engineering, Faculty of Science Engineering and Built Environment, Deakin University, Geelong, Australia

ARTICLE INFO

Keywords:

Wood
Basalt fibre
Hybrid wood-basalt laminates
Crushing
Crashworthiness

ABSTRACT

In the pursuit of sustainable material solutions for future transport vehicles, thin-walled wood veneers and Basalt Fibre Reinforced Polymers (BFRPs) present viable options. Given that crashworthiness is a critical property in the design of safe and reliable structures, this paper investigates the mechanical behaviour of wood veneers, BFRPs, and hybrid combinations when subjected to quasi-static axial crush tests. As expected, the results show that BFRPs can absorb significantly more energy, with Specific Energy Absorption (SEA) values of 48 kJ/kg, up to three times higher compared to pure wood veneer laminates. The results of the hybrid material combinations demonstrate the critical role of bonding between the wood veneers and BFRP, with splaying identified as the dominant failure mode. Debonding fracture tests and the simulations of the pressing process during manufacturing confirm that non-uniform pressure along the curved, omega-shaped test samples should be avoided. It is shown that mitigating splaying in hybrid wood-BFRP samples leads to SEA values of 40 kJ/kg, which is approximately double the values observed when debonding/splaying is present. These findings are important in designing sustainable hybrid material solutions while optimising for crashworthiness.

1. Introduction

Wood is recognised for its low energy requirements in the manufacturing of various products such as veneers or sawn boards. Moreover, the biogenic nature of wood makes it a carbon negative material [1,2]. With the advancement of mass engineered wood products, e.g., laminated veneer lumber and glue/cross laminated timber, the use of wood for structural engineering applications has reached new dimensions in recent years. Mass engineered wood products are now being employed in mid to high rise buildings and bridges. Furthermore, wood is considered a suitable and desirable alternative in aviation and automotive applications. For instance, the French company Aura-Aero [3] is currently offering light aircraft structures partially made from wood.

Similar to wood, natural fibre-based composites have many attractive properties, particularly in relation to sustainability and recyclability [4]. In the automotive industry, natural fibre-based composites made from hemp and flax fibres are being used for exterior components by Porsche, while Audi employs flax and sisal fibre mats as elements of door trim. Furthermore, BMW has replaced fibreglass composites with flax and sisal fibres for interior door linings [4–6].

In transport applications, ensuring crashworthiness is of utmost importance. Crashworthiness is defined as the capacity of materials and structures to absorb energy induced by an impact. Materials with good crashworthiness properties can dissipate kinematic energy efficiently through controlled crush mechanisms, thereby enhancing passenger safety. The primary characteristics of crashworthiness are measured by failure modes, specific energy absorption (SEA), and crush efficiency (CE) [7–9].

Pure wood and wood-based veneers have been investigated for their crashworthiness [10]. Pure solid cylindrical wood (*Toona Sinensis*) was tested along longitudinal, radial and tangential directions, with SEA values of approximately 10 kJ/kg [11]. In addition, the crashworthiness of wood veneers was studied in [12–14]. Various stacking sequences of Poplar were investigated [13], with average reported SEA values of 30 kJ/kg for hollow cylindrical tubes. Natural fibre composites under axial crushing of circular hollow tubes, including flax, jute and kenaf fibres, achieved SEA values between 18 – 28 kJ/kg [15,16], 12 – 25 kJ/kg [17,18], and 18 kJ/kg [19], respectively.

In aiming at synergistically enhanced material properties, numerous hybrid material solutions have been investigated with respect to

* Corresponding author.

Email address: johannes.reiner@deakin.edu.au (J. Reiner).

crashworthiness [20]. Many of these studies have focused on the combination of natural fibres with synthetic fibres such as Glass Fibre Reinforced Polymers (GFRP) and Carbon Fibre Reinforced Polymers (CFRP). Examples include jute-glass-carbon [17], kenaf-glass [21], flax-glass [22], wood-filled CFRP tubes [11], balsa-CFRP and balsa-GFRP [23], Poplar-CFRP and Poplar-GFRP [14]. The improvements in SEA are highly dependent on the stacking sequences. For certain stacking sequences, a maximum of approximately 50 % improvement in SEA was observed for hybrid tubes compared to those made from pure wood or natural fibre-based composites.

While these studies demonstrate the potential for producing hybrid material systems with enhanced energy-absorbing properties, they all incorporate synthetic fibres. To investigate sustainable hybrid materials with a low carbon footprint, the present study combines thin wood veneers with Basalt Fibre Reinforced Polymer (BFRP) laminates [24] subjected to axial crush tests. In many structural applications, the stiffness of pure wood materials is insufficient [25], and thus the addition of natural fibre-based composites in form of BFRP has the potential to enhance the stiffness while maintaining a sustainable material solution with a low carbon footprint [26]. Fernando et al. [27] reported that the incorporation of BFRP with wood can enhance axial stiffness and strength by up to 26 % and 65 %, respectively. Thorhallsson et al. [28] observed an increase in bending strength of glulam beams by 37 – 57 % when reinforced with BFRP mats. While the improvements in stiffness and strength of wood through the integration of BFRP have been documented, the energy absorption capacity of wood-BFRP composites remains unexplored.

This paper presents the investigated material types and manufacturing processes in [Section 2](#), followed by the analysis of qualitative and quantitative results obtained from debonding fracture tests in [Section 3](#) and axial crush tests in [Section 4](#). These results are discussed in [Section 5](#) with a particular focus on the applicability of a simple analysis technique, the rule of mixtures, for estimating the crush behaviour of hybrid wood-BFRP material configurations. [Section 6](#) concludes this study with potential implications and immediate future work. To the best knowledge of the authors, the present study is the first to examine the crashworthiness of hybrid wood-BFRP laminates, thereby establishing a foundation for the use of sustainable, energy-absorbing materials in future transport applications.

2. Materials, manufacturing and testing

This study investigates the crush behaviour of pure wood veneers, pure BFRP laminates, and combinations of the two material systems, with particular focus on the interface between the dissimilar materials. This section outlines the individual material types, as well as the manufacturing, testing and analysis of the laminates subjected to debonding fracture and quasi-static axial crush tests.

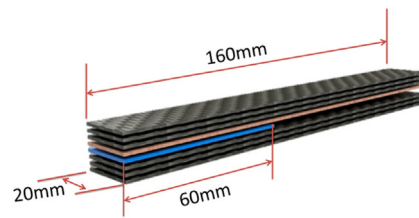


Fig. 1. Geometry and dimensions of test specimen for debonding fracture testing of hybrid wood-BFRP materials.

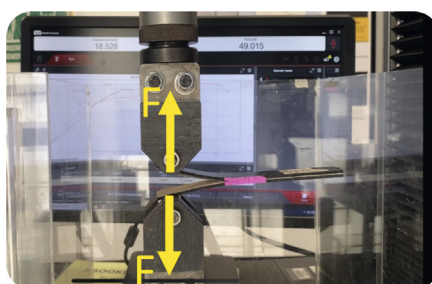
2.1. Wood veneers and basalt fibre reinforced polymers

The test specimens were made from 600 g/m² biaxial Basalt Fibre fabrics (DB600) and 0.6 mm thick rotary-cut European Beech veneers procured from Basalt Fiber Tech, Oakleigh, VIC, Australia and Metz & Co, Stuttgart, Germany, respectively.

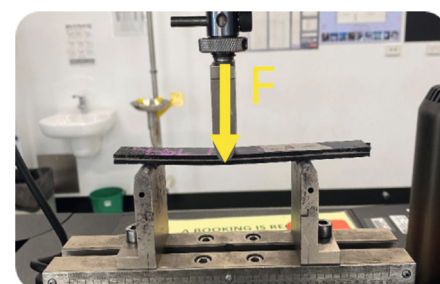
2.2. Debonding fracture tests

As bonding between wood and BFRP is anticipated to be a major concern, standardised interlaminar fracture tests were conducted to quantify the bonding between these two dissimilar materials. The tests followed the ASTM standards D5528 and D7905 for Mode I and Mode II fracture, respectively. [Fig. 1](#) illustrates the layup and the dimensions of a hybrid test specimen. Two [0/90]₃ BFRP sub-laminates were stacked with a single [0] wood veneer ply interposed. The 0° orientation runs along the length of the test sample. For the [0/90]₃ BFRP sub-laminates, the dry basalt fabrics were impregnated at a 50 % weight ratio by combining West Systems 105 epoxy resin with 206 hardener. The impregnated laminates were cured for a minimum of 24 hours in a fume hood, without the application of external pressure. The [0] wood veneer ply was bonded to the BFRP sub-laminates by applying 140–180 g/m² of one component polyurethane (Purbond HB S109). A 60 mm long Teflon sheet was inserted on the surface between the wood veneer and one BFRP sub-laminate to initiate debonding failure. To investigate the effects of pressure and pressing time, hybrid panels were pressed at 0.5 and 1.0 MPa over durations of 10, 20 and 75 minutes. The recommended manufacturing parameters for wood-to-wood bonding with Purbond HB S109 are 0.6–1.0 MPa of pressure over a pressing time of 25–75 min [29]. After curing, the hybrid panels were cut to the sample dimensions shown in [Fig. 1](#).

The Mode I and Mode II fracture tests were conducted on a 10 kN Instron load frame, with loading rates of 2 mm/min and 0.5 mm/min, respectively. The double cantilever beam specimen for Mode I testing shown in [Fig. 2\(a\)](#) requires the bonding of two aluminium blocks, which are attached to the load frame via pins. Mode II debonding is initiated through three-point bending as depicted in [Fig. 2\(b\)](#).



(a) Mode I



(b) Mode II

Fig. 2. Fracture testing of hybrid wood-BFRP material to measure bonding between the dissimilar materials.

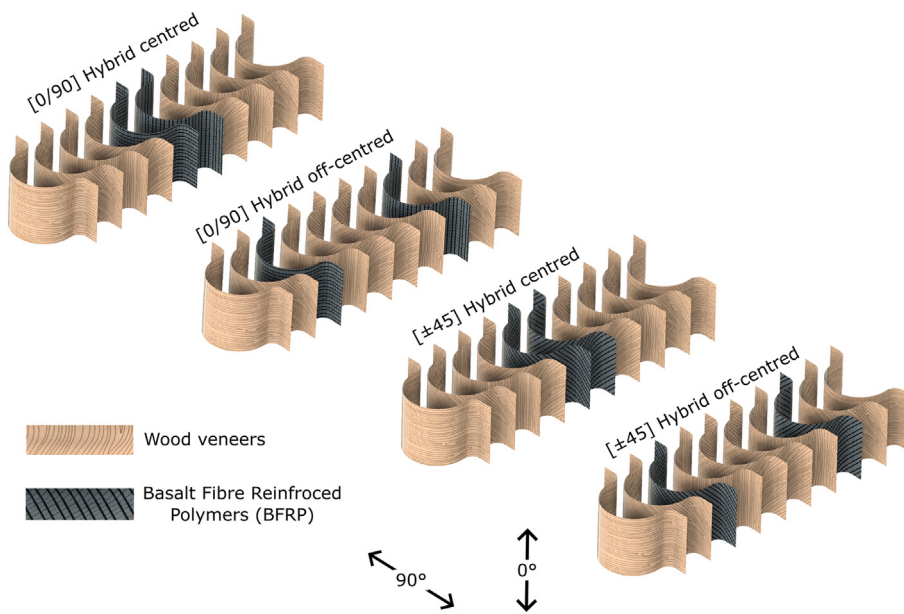


Fig. 3. Overview of investigated omega-shaped hybrid laminates made from quasi-isotropic [90/45/0/-45]_s wood veneers and BFRP laminates, varying location and orientation of BFRP plies.

To quantify the energy required for debonding between the wood veneer and the BFRP sub-laminates, the energy release rates G can be calculated. By measuring the resultant forces F and the prescribed displacement δ obtained from the loading machine, as well as the debonding length Δa , the Mode I and Mode II fracture energies can be determined by

$$\begin{aligned} G_I &= \frac{3F\delta}{2b(a + \Delta)} \\ G_{IIc} &= \frac{3mF_{\max}a_0^2}{2b} \end{aligned} \quad (1)$$

with the initial debonding length $a_0 = 60$ mm, total debonding length $a = a_0 + \Delta a$, and specimen width $b = 20$ mm. The correction factor Δ is determined as the intercept of the plot of the cube root of the specimen compliance against the crack length Δa . The factor m in the calculation of G_{IIc} represents the slope of the linear fit of compliance versus crack length cubed data. Note that the Mode I fracture energy to initiate debonding (at $\Delta a = 0$) is referred to as the critical Mode I fracture energy G_{Ic} .

2.3. Axial crush tests

In addition to pure material configurations comprising quasi-isotropic [90/45/0/-45]_s wood veneer laminates and cross-ply [0/90]_{4s} and [±45]_{4s} BFRP laminates, a range of hybrid combinations was considered for the axial crush tests. The range of these combinations is illustrated in Fig. 3 with differently oriented thin [0/90]_s BFRP plies and varying locations within the quasi-isotropic wood veneer laminates. The orientation refers to the loading direction during axial crushing. The 0° orientation aligns with the height of each test sample.

Manufacturing

Previous studies by the authors have explored various manufacturing techniques to produce flat wood veneer laminates [29–31], similar to the manufacturing process described in Section 2.2. In the present study, the omega-shaped test samples depicted in Fig. 3 require a more complex manufacturing procedure due to their curved geometry. The omega shape in Fig. 4 is based on previous work conducted by the German Aerospace Center (DLR) [32] on carbon fibre reinforced polymers, and ensures stable crushing of relatively small composite structures. Here,

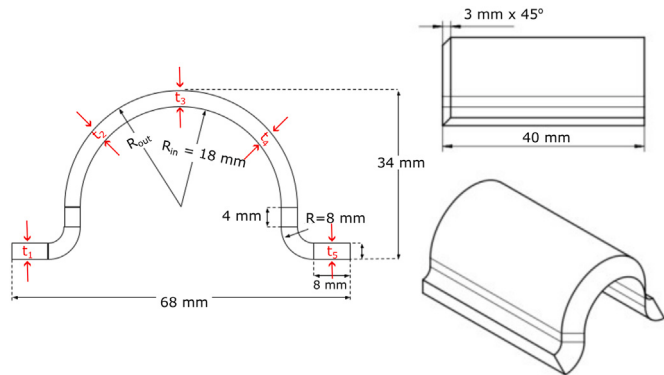


Fig. 4. Illustration and dimensions of omega-shaped axial crush test sample, including chamfer trigger to ensure stable axial crushing. The locations $t_x, x = 1, \dots, 5$ refer to thickness measurements along the cross-section of the test sample.

the inner radius $R_{in} = 18$ mm is fixed, while the outer radius R_{out} varies depending on the manufactured material combinations and typically ranges between 22 mm and 24 mm.

The major steps for manufacturing the wooden omega shapes are depicted in Fig. 5. For each wooden specimen, eight pieces of 110 mm × 110 mm Beech wood veneers were cut, with four pieces oriented at 0°/90° grain direction and four at ±45° grain direction. To facilitate smooth forming into the omega shape geometry, the veneers were placed into a container connected to a Wagner SteamForce wallpaper steamer for 90 seconds. M8 nuts were used as spacers between the layers to ensure uniform moisture absorption by the veneers. The wet and conditioned veneers were formed individually in the layup sequence of [90/45/0/-45]_s, without the application of any adhesive. The stack was placed in a hydraulic press at 1 MPa pressure for at least 12 hours and subsequently dried in an oven at 30 °C for 15 minutes to eliminate any remaining surface moisture. Once dried, the formed veneers were separated, and 2 g of one component polyurethane (Purbond HB S109) adhesive was evenly applied to their surfaces. Teflon sheets were placed

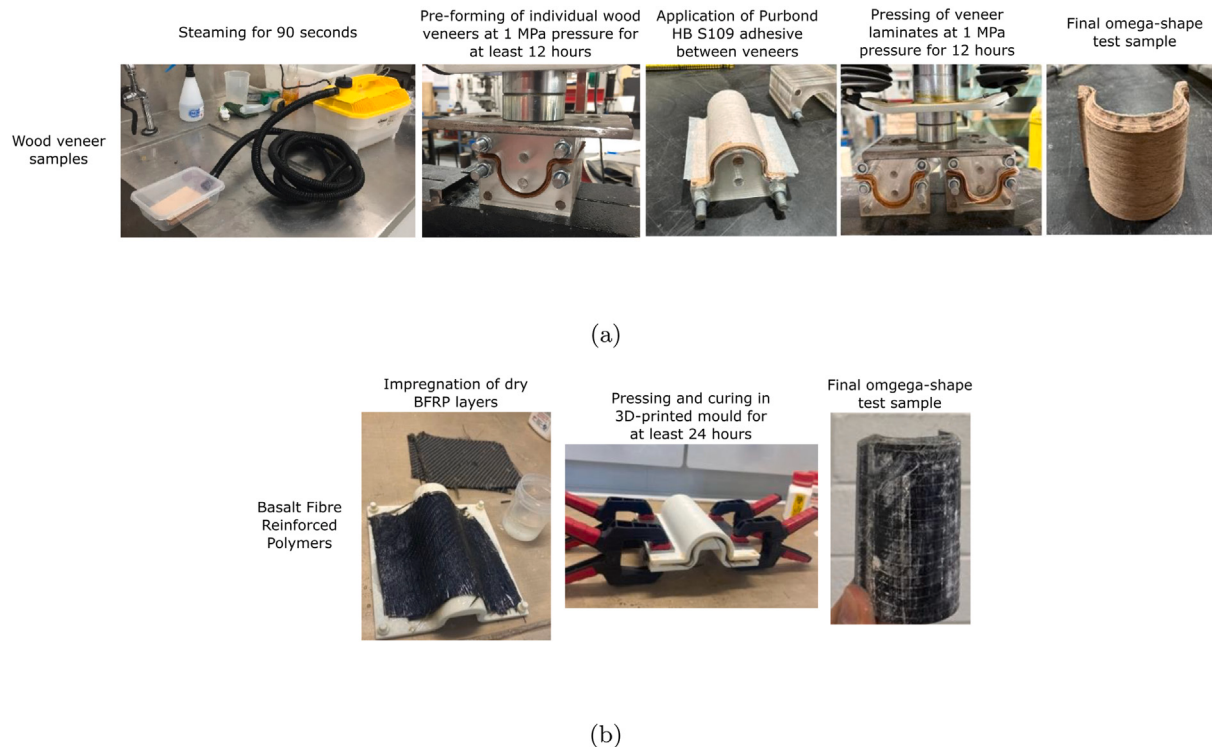


Fig. 5. Illustration of manufacturing processes to produce omega-shaped crush specimens made from (a) wood veneers and (b) BFRP laminates.

on the mould surfaces, after which the adhesive-coated veneers were placed in the mould and pressed at 1 MPa for 12 hours.

For the pure BFRP samples, the dry basalt layers were impregnated at a 50 % weight ratio by combining West Systems 105 epoxy resin with 206 hardener, see Fig. 5. The pure BFRP specimens were pressed in a 3D printed mould, with each layer being wet (uncured), then stacked on the male mould. The female mould was placed on top, then clamped and left to cure for a minimum of 24 hours.

The manufacturing of the hybrid configurations followed a similar, albeit more time-consuming procedure. Initially, the wood veneers were pressed at 1 MPa for 12 hours with spacers being positioned at the location of the BFRP plies to ensure appropriate curvatures of individual sheets. After the application of the adhesives to the wood veneers, Teflon sheets were inserted within the wood layup at the location of the BFRP plies. The impregnated basalt sheets were then placed on these Teflon sheets. This assembly was pressed at 1 MPa for 24 hours to fully cure the epoxy resin in the required omega shape. Upon full curing of the BFRP, 2 g of Purbond HB S109 adhesive was applied to both sides of the BFRP plies to bond them to the wood veneer laminates. The stack was pressed at 1 MPa for an additional 12 hours to complete curing of the hybrid test samples.

For all the test samples, a tile cutter was used to remove the sides and cut the specimens into 40 mm-long segments, see Fig. 4. A 45° chamfer was cut into one of the outside edges to induce stable crushing during testing.

Testing

The static axial crush tests of the omega-shaped samples were carried out on a 300 kN Instron universal testing machine with a cross-head displacement rate of 1 mm/min. As illustrated in Fig. 6, a 10 mm high stabiliser was used to prevent slipping of the test samples and to improve the overall buckling resistance. The prescribed displacement was applied over a total crush distance of 20 mm. During the crush tests, the deformation of the specimens was monitored through visual inspection and recorded via a time-lapse camera. In addition, the testing machine recorded the applied displacement δ and the resultant force F .

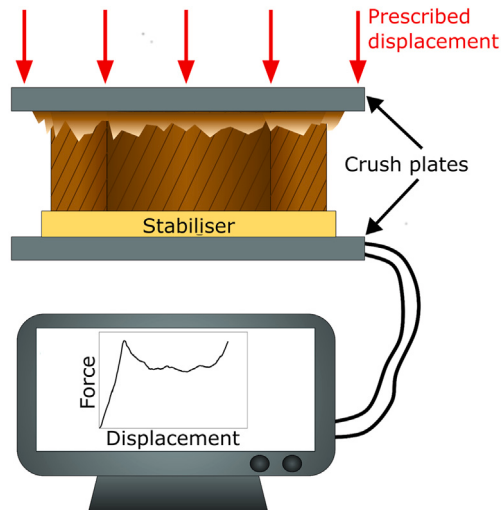


Fig. 6. Illustration of axial crush test and recording of force vs displacement data for the evaluation of energy-absorbing properties.

The measured force F and displacement δ enable the calculation of the Specific Energy Absorption (SEA), a measure of how well the tested materials can absorb energy during crushing. It takes into account the density ρ of the material and the crushed cross-sectional area A such that

$$\text{SEA} = \frac{\int_{\delta_1}^{\delta_2} F d\delta}{\rho A(\delta_2 - \delta_1)}, \quad (2)$$

where δ_1 and δ_2 denote the crushed length at peak force F_{\max} and the maximum crush length related to stable crushing, respectively. These

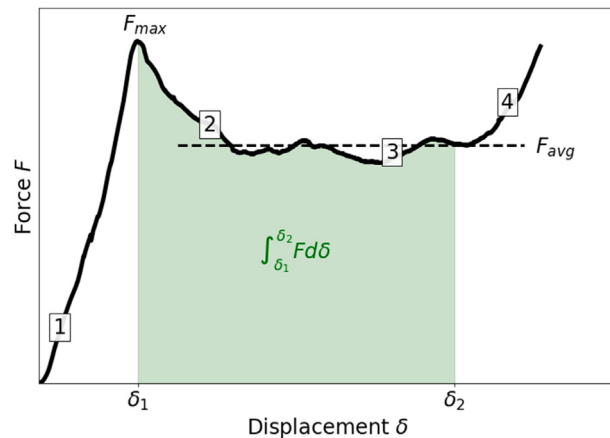


Fig. 7. Explanation of typical measurements in force vs displacement graph obtained from axial crush testing. The numbers in white squares \boxed{i} , $i = 1, \dots, 4$ refer to different instants during axial crushing shown in Fig. 8.

values are illustrated in Fig. 7 showing a typical force vs displacement result from one of the axial crush tests. Stable crushing relates to the force plateau in the graph. The SEA value measures the area under the force response during stable crushing ($\int_{\delta_1}^{\delta_2} F d\delta$), normalised by the crushed mass ($\rho A(\delta_2 - \delta_1)$). Note that the density ρ of hybrid configurations, consisting of materials 1 and 2, is the sum of the individual densities ρ_1 and ρ_2 . The Crush Efficiency (CE) is another measurement, and is defined by

$$\text{CE} = \frac{F_{\text{avg}}}{F_{\text{max}}} \quad (3)$$

with F_{avg} being the constant force during stable crushing. CE measures the forces transmitted through the impacted material. High CE values indicate that lower forces will be transmitted to surrounding components (e.g., passengers in vehicles), which can be used to assess the risk of head and neck injuries during a collision.

Fig. 8 shows a typical testing sequence, where the numbers in the top left corner correspond to four characteristic instants during axial crushing highlighted in the force vs displacement graph in Fig. 7. In this example, it can be seen that the crush forces increase during the crushing of the chamfer trigger between instants $\boxed{1}$ and $\boxed{2}$. The maximum crush force F_{max} coincides with the complete crushing of the trigger zone. Stable crushing occurs between instants $\boxed{2}$ and $\boxed{3}$, resulting in a relatively constant force response. As the loading plate approaches the stabiliser, the measured force increases due to the influence of factors other than crush-related measurements, such as contact between the crushed test sample and the stabiliser, potentially resulting in additional deformation.

There are two major failure modes during axial crushing of composite materials, namely fragmentation and splaying. Fig. 9 illustrates these two failure modes. During fragmentation, the fibres are pulverised, resulting in a high amount of absorbed energy. In contrast,

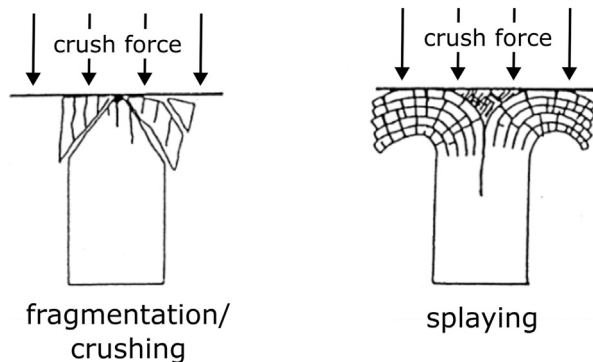


Fig. 9. Illustration of typical failure modes in composites subjected to axial crushing, adopted from [33].

Table 1

Average specimen thickness (in mm) prior to Mode I and Mode II fracture testing.

	Pressure	Pressing time		
		10 min	20 min	75 min
0.5 MPa		5.95	5.58	5.63
1.0 MPa		5.66	5.41	5.48

splaying is initiated by interlaminar damage, where the separation of layers leads to significantly less absorbed energy. Generally, fragmentation is the desired failure to optimise energy absorption; however, it also increases the risk of unstable buckling and catastrophic failure.

3. Results: debonding fracture tests

The Mode I and Mode II debonding tests were conducted on test samples subjected to different manufacturing processes by varying pressure (0.5 MPa and 1.0 MPa) and pressing time (10, 20 and 75 minutes). A minimum of three tests were analysed for each manufacturing process. Prior to testing, the thickness of each specimen was measured. Table 1 lists the average thickness measurements corresponding to each manufacturing process. It can be seen that higher pressure of 1.0 MPa combined with longer pressing times (20 and 75 minutes) leads to thinner samples.

Fig. 10(a) shows examples of force vs displacement curves and crack (debonding) length measurements of three samples manufactured at 1.0 MPa over 75 minutes. Generally, the peak of the force vs displacement curve coincides with the onset of debonding. The data on force F , displacement δ and crack length Δa enable the application of Equations (1) to determine the critical Mode I and Mode II fracture energies G_c . The bar charts in Fig. 10(b) depict the average fracture energies, alongside standard deviations represented by error bars. It can be seen that longer pressing times yield increased fracture energies, indicating enhanced bonding between the wood veneer and BFRP sub-laminates. This trend is more pronounced in the results from samples manufactured

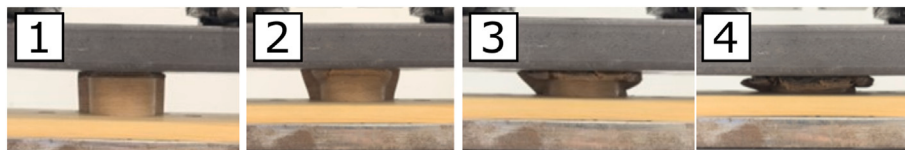


Fig. 8. A hybrid wood-BFRP laminate under axial crush testing. The instants \boxed{i} , $i = 1, \dots, 4$ refer to the force vs displacement graph shown in Fig. 7.

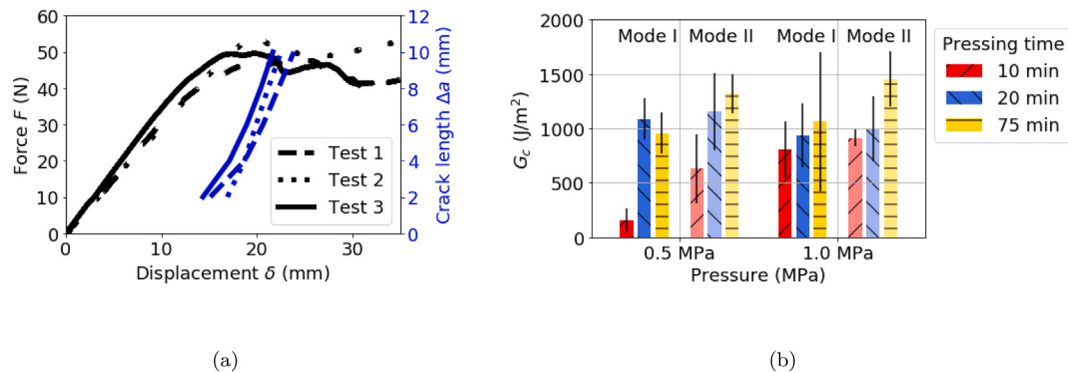


Fig. 10. Results from debonding fracture testing of hybrid wood-BFRP laminates. (a) Examples of force vs displacement curves and crack length measurements from samples manufactured at 1.0 MPa for 75 minutes, and (b) comparison of critical fracture energies G_c in Mode I and Mode II fracture tests.

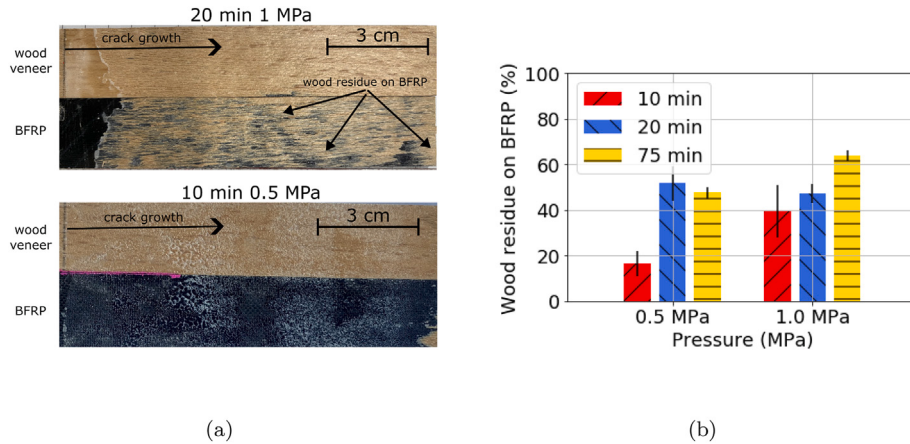


Fig. 11. (a) Qualitative and (b) quantitative analysis of wood residue on BFRP plies after Mode I debonding fracture testing.

at lower pressure of 0.5 MPa, highlighting the importance of pressure during the manufacturing of hybrid wood-BFRP composites. A closer look at the interface after testing in Fig. 11(a) reveals the presence of wood residue on BFRP for samples with high fracture energy evaluations, such as those manufactured at 1.0 MPa over 20 minutes. In contrast, the shortest manufacturing duration of 10 minutes at the lowest pressure of 0.5 MPa results in interfaces without noticeable wood residue. To further quantify these observations, Fig. 11(b) compares wood residue on BFRP after Mode I testing across all investigated manufacturing processes. A Matlab code converted the original coloured interface images from the BFRP side into black-and-white, enabling the measurement of the ratio between black (BFRP) and white (wood) pixels. The percentages of wood residue shown in Fig. 11(b) are consistent with the trends observed in the Mode I fracture energy measurements from Fig. 10(b), with low pressure and pressing time leading to reduced bonding quality. These findings will play a key role in understanding the results obtained from the axial crush tests of the hybrid wood-BFRP specimen.

4. Results: axial crush tests

In the following, qualitative and quantitative measures from the quasi-static axial crush tests will be analysed based on specimens made from pure wood veneers and pure BFRP laminates, as well as the hybrid combinations depicted in Fig. 3. A minimum of three specimens of each material configuration were tested and analysed. First, the thickness variations before testing and the characteristic failure modes after testing will be presented, followed by the measured force vs displacement curves and the resultant quantities pertaining to SEA and CE. A comparative discussion of these results will be provided in Section 5.

4.1. Thickness measurements

Similar to the analysis of the debonding results in Section 3, thickness measurements were performed prior to conducting axial crush tests. Table 2 lists the representative thickness values measured at various locations along the cross-section of the omega-shaped test samples for the different hybrid configurations. Fig. 4 illustrates these five locations. It can be seen that the samples at locations t_2 and t_4 are consistently thicker compared to the other three locations, suggesting inconsistencies in the manufacturing process of the test samples. This observation will help explain the results observed from the axial crush tests on hybrid samples presented in Section 5.

4.2. Failure modes

Fig. 12(a) and (b) present the omega-shaped specimens made from pure wood veneers and pure BFRP, respectively, after axial crush testing. While the BFRP sample shows a combination of expected failure

Table 2

Thickness measurements (in mm) at different locations along the cross-section of the omega-shaped crush samples, see Fig. 4.

Location	[0/90] centred	[±45] centred	[0/90] off-centred	[±45] off-centred
t_1	4.59	4.23	5.71	5.75
t_2	6.20	5.39	5.97	6.21
t_3	4.16	4.39	5.65	5.88
t_4	6.16	6.21	6.12	6.16
t_5	4.33	4.58	5.72	5.80



(a) Wood veneers

(b) $[0/90]_{4s}$ BFRP laminates

Fig. 12. Examples of omega-shaped samples made from pure materials (wood and BFRP) after axial crush testing.

modes characteristic of crushed composites, namely splaying and fragmentation, the crushed zone of the wood veneers is confined to a narrow region, with the majority of the wood undergoing densification.

It is not trivial to anticipate the dominant failure modes of the hybrid combinations, and whether the observed failure modes depend upon the through-thickness location of the BFRP layers and/or the orientation of the BFRP laminates. Fig. 13 shows some examples of the observed failure modes in the hybrid crush samples with $[0/90]$ centred and off-centred BFRP plies, as well as $[\pm 45]$ centred plies. The majority of these samples exhibit severe debonding between the two dissimilar materials, wood veneers and BFRP laminates, resulting in significant splaying. In these instances, the failure modes of the individual material sections resemble those observed in the crush tests of pure materials shown in Fig. 12. A closer look at the areas of splaying reveals minimal to no wood residue on the BFRP laminates, suggesting a weak bond between the two dissimilar materials. Additionally, it can be seen that the regions of severe debonding are concentrated around the curved sections of the omega-shaped test samples, where thickness measurements t_2 and t_4 were conducted, see Table 2. A few hybrid samples also showed evidence of local buckling, as depicted in Fig. 13(c). The failure modes in Fig. 13 showing debonding as the dominant failure mode were consistent for all tested samples within these three hybrid configurations. In contrast, Fig. 14 shows that the failure modes observed in the hybrids with $[\pm 45]$ off-centred BFRP plies are less consistent. Two out of the four test samples (① and ②) show severe debonding, similar to the failure modes observed in the other hybrid configurations depicted in Fig. 13.



Fig. 14. Failure modes observed in all four tested hybrid wood-BFRP laminates with $[\pm 45]$ off-centred BFRP plies. The circled numbers in the top left corner refer to the measured force vs displacement graphs shown in Fig. 18(b).

However, the other two samples (③ and ④) did not exhibit a significant amount of separation between the wood-BFRP interfaces, resulting in a smooth crush surface. The observations regarding the failure modes will inform the discussion of the range of quantitative results presented in the subsequent sub-sections.

4.3. Wood veneers

The force vs displacement graphs obtained from the axial crush tests of pure quasi-isotropic wood veneers are presented in Fig. 15. The peak crush forces are observed to be within the range of 6–8 kN. Equations (2) and (3) can be used to calculate SEA and CE, respectively. Table 3 summarises these results. Notably, the mean SEA value is 15.25 kJ/kg with a coefficient of variation (cv) of 7.2 %.

4.4. Basalt fibre reinforced polymers

The two pure BFRP configurations $[0/90]_{4s}$ and $[\pm 45]_{4s}$ consist of samples where the basalt fibres are aligned with the crush load direction $[0/90]$ and rotated by 45° , respectively. Fig. 16(a) and (b) show the resulting force vs displacement graphs obtained from three tests of each configuration. The $[0/90]_{4s}$ BFRP laminates in Fig. 16(a) exhibit high forces during progressive crushing with values ranging from 30 to 45 kN. No distinct peak forces are observable before the force plateau initiates at approximately 3 mm of crush distance. In contrast, the graphs of the $[\pm 45]_{4s}$ BFRP laminates shown in Fig. 16(b) display peak crush forces

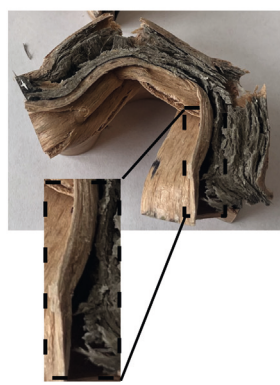
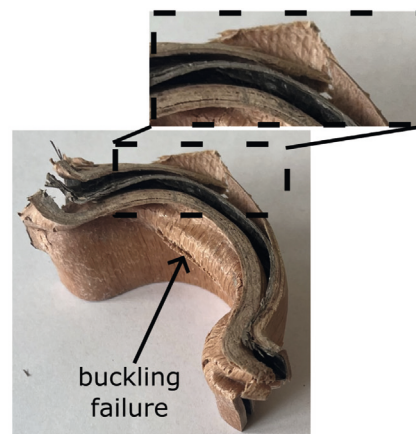
(a) $[0/90]$ centred(b) $[0/90]$ off-centred(c) $[\pm 45]$ centred

Fig. 13. Hybrid wood-BFRP samples after axial crush testing, showing severe splaying due to debonding. A closer look at the interfaces reveal minimal to no wood residue on BFRP plies.

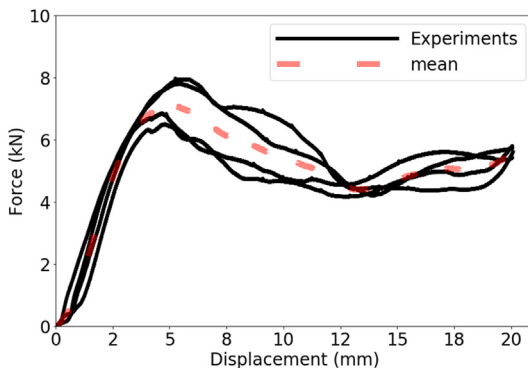


Fig. 15. Force vs displacement graphs obtained from axial crush tests of pure wood veneers.

Table 3

Summary of calculated crush properties of pure wood veneers, including mean values and coefficients of standard deviation (cv).

	Sample 1	Sample 2	Sample 3	Sample 4	Mean (cv)
SEA (kJ/kg)	16.11	16.52	13.99	14.36	15.25 ($\pm 7.2\%$)
Crush efficiency (-)	0.68	0.69	0.68	0.72	0.69 ($\pm 2.4\%$)

of 25 to 35 kN with marginally decreasing post-peak forces during progressive crushing. **Table 4** lists the quantitative crush properties, SEA and CE, of each BFRP test sample. Considering the mean SEA value of 47.99 kJ/kg, it can be seen that the [0/90]_{4s} laminates absorb 61 % more energy compared to the [±45]_{4s} laminates. The coefficients of variation are comparable at approximately 15–17 %.

4.5. Hybrid wood-BFRP configurations

The quantitative results of the hybrid configurations shown in **Fig. 3** are grouped according to the position of the BFRP layers relative to the wood veneers. **Fig. 17** shows the force vs displacement graphs obtained from hybrid samples with centrally located BFRP layers, while **Fig. 18** shows the results from test samples with off-centred BFRP layers.

The graphs of the two hybrid configurations with centred BFRP layers in **Fig. 17** are similar, with peak crush forces ranging between 15 kN and 20 kN. The graphs obtained from the [0/90] BFRP laminates shown in **Fig. 17(a)** display slightly higher post-peak forces with greater variability compared to the [±45] counterpart in **Fig. 17(b)**. The hybrid laminates with off-centred [0/90] BFRP plies in **Fig. 18(a)** exhibit a response comparable to the centred configurations in **Fig. 17(a)**. However, two out of

Table 4

Summary of calculated crush properties of pure [0/90]_{4s} and [±45]_{4s} BFRP laminates, including mean values and coefficients of standard deviation (cv).

	Sample 1	Sample 2	Sample 3	Mean (cv)
[0/90] _{4s} BFRP laminates				
SEA (kJ/kg)	39.53	58.59	45.85	47.99 ($\pm 16.5\%$)
Crush efficiency (-)	0.69	0.84	0.73	0.75 ($\pm 8.4\%$)
[±45] _{4s} BFRP laminates				
SEA (kJ/kg)	24.07	29.57	35.45	29.70 ($\pm 15.6\%$)
Crush efficiency (-)	0.49	0.65	0.67	0.60 ($\pm 13.3\%$)

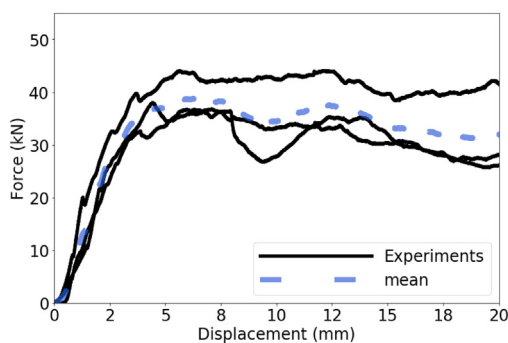
the four test samples with the off-centred [±45] BFRP plies in **Fig. 18(b)** yield higher force levels, with peak forces ranging between 25 kN and 30 kN.

Tables 5 and **6** present the SEA and CE calculations obtained from each crush test of hybrid configurations with centred and off-centred BFRP plies, respectively. It can be seen that the two hybrids with centred and off-centred [0/90] BFRP plies yield comparable results, with SEA values of 26.52 kJ/kg and 26.81 kJ/kg, respectively. The hybrids with centred [±45] BFRP plies exhibit lower post-peak forces, resulting in a reduced mean SEA value of 18.91 kJ/kg. The higher crush forces of the hybrids with off-centred [±45] BFRP plies yield the highest energy absorbing measures, with a mean SEA of 33.18 kJ/kg. In addition, the two tables demonstrate that the crush efficiencies for the off-centred configurations are 0.74–0.75, while the centred versions yield values up to 27 % lower.

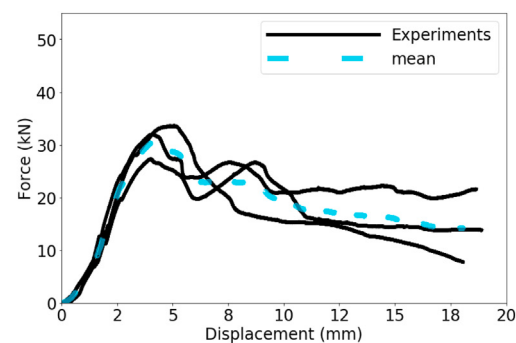
As a summary, **Fig. 19** presents the measured mean SEA values for each material configuration, alongside error bars determined by the calculated coefficients of variation. It can be seen that the centred hybrid configurations follow the trend observed in the pure BFRP materials, wherein the [0/90] laminates absorb significantly more energy compared to the [±45] counterparts. Conversely, the off-centred hybrid materials display an inverse trend, with [±45] BFRP plies absorbing more energy compared to the [0/90] laminates. The following **Section 5** provides a detailed analysis of these results, including guidelines for the manufacturing, design and analysis of energy-absorbing hybrid wood-BFRP laminates.

5. Discussion

The discussion of the results in **Section 4** and their comparison will focus on the question of whether the testing and analysis of pure wood veneers and BFRP laminates are sufficient to design hybrid configurations. Furthermore, manufacturing and design related investigations will help explain these findings.



(a) [0/90]_{4s} BFRP laminates



(b) [±45]_{4s} BFRP laminates

Fig. 16. Force vs displacement graphs obtained from axial crush tests of pure BFRP laminates.

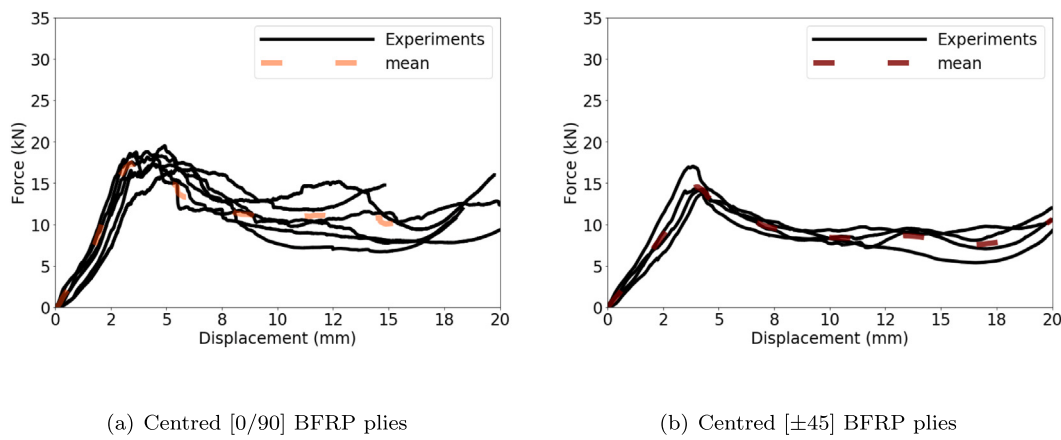


Fig. 17. Force vs displacement graphs obtained from axial crush tests of hybrid wood-BFRP laminates with centred BFRP plies, see Fig. 3.

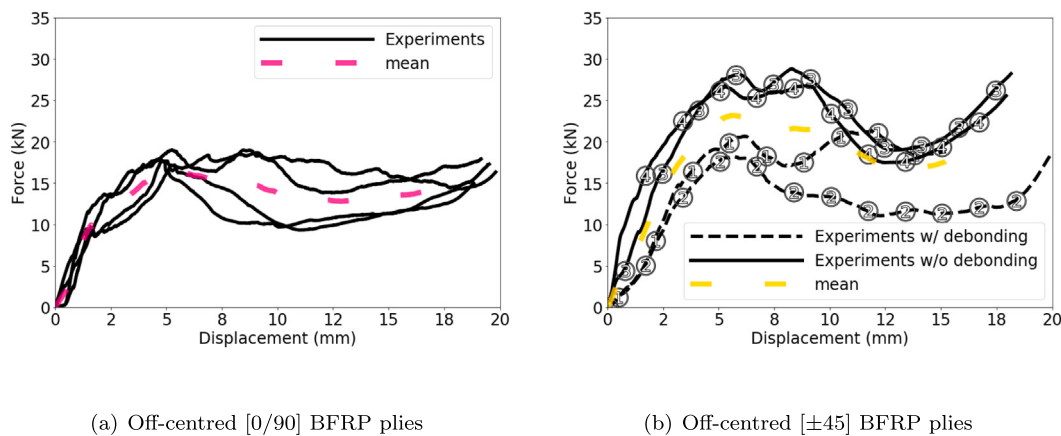


Fig. 18. Force vs displacement graphs obtained from axial crush tests of hybrid wood-BFRP laminates with off-centred BFRP plies, see Fig. 3. The circled numbers in (b) refer to the samples shown in the failure analysis in Fig. 14.

Table 5

Summary of calculated crush properties of hybrid wood-BFRP laminates with centred BFRP plies, including mean values and coefficients of standard deviation (cv).

	Sample 1	Sample 2	Sample 3	Sample 4	Mean (cv)
Hybrid wood-BFRP with centred [0/90] BFRP plies					
SEA (kJ/kg)	27.71	31.29	26.55	20.52	26.52 ($\pm 14.6\%$)
Crush efficiency (-)	0.71	0.63	0.63	0.56	0.63 ($\pm 8.4\%$)
Hybrid wood-BFRP with centred [±45] BFRP plies					
SEA (kJ/kg)	20.20	19.96	18.78	16.69	18.91 ($\pm 7.3\%$)
Crush efficiency (-)	0.54	0.59	0.66	0.58	0.59 ($\pm 7.3\%$)

In aiming at a simple and efficient design solution, the following section will investigate the extent to which the rule of mixtures can be utilised to estimate the crush performance of hybrid structures. If r is the proportion of BFRP material within a hybrid configuration, then the rule of mixtures estimates a property p_{Hybrid} of the hybrid structure by taking into account the properties obtained from the pure wood p_{Wood} and BFRP materials p_{BFRP} such that

$$p_{\text{Hybrid}} = r * p_{\text{BFRP}} + (1 - r) * p_{\text{Wood}}. \quad (4)$$

The investigated properties p will be force vs displacement graphs, as well as SEA and CE values.

Table 6

Summary of calculated crush properties of hybrid wood-BFRP laminates with off-centred BFRP plies, including mean values and coefficients of standard deviation (cv).

	Sample 1	Sample 2	Sample 3	Sample 4	Mean (cv)
Hybrid wood-BFRP with off-centred [0/90] BFRP plies					
SEA (kJ/kg)	22.07	20.13	33.18	31.87	26.81 ($\pm 21.5\%$)
Crush efficiency (-)	0.67	0.62	0.89	0.78	0.74 ($\pm 14.1\%$)
Hybrid wood-BFRP with off-centred [±45] BFRP plies					
SEA (kJ/kg)	31.49	22.36	40.54	38.35	33.18 ($\pm 21.3\%$)
Crush efficiency (-)	0.78	0.66	0.76	0.80	0.75 ($\pm 7.2\%$)

5.1. Comparison of results

The force vs displacement graphs from the previous section are compared with each other. Fig. 20 presents the mean of these graphs, as well as their variation mean \pm standard deviation (std). The graphs of the pure materials in Fig. 20(a) demonstrate the significant differences between the wood veneers and the BFRP laminates. While the axial crushing of BFRP laminates results in 4–5 times larger forces, the wood veneers show more consistent crush behaviour with limited variations. This observation is further supported by Tables 3 and 4, where the standard deviations of SEA and CE in wood veneers are approximately half compared to pure BFRP laminates. The comparison of the

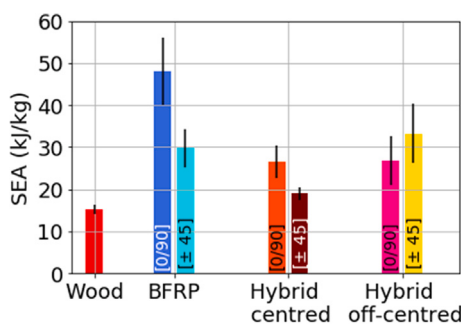


Fig. 19. Comparison of Specific Energy Absorption (SEA) measured from axial crush tests of pure wood veneers and BFRP laminates, as well as hybrid combinations with varying location and orientation of BFRP plies.

force vs displacement graphs obtained from the hybrid materials in Fig. 20(b) shows a relatively consistent crush response, with the exception of higher crush forces resulting from hybrids with [±45] off-centred BFRP plies. Similarly, the extent of variations within each configuration is comparable. The laminates with [±45] centred BFRP plies show the most consistent responses, confirmed by a low cv value for SEA of 7.3 % as shown in Table 5.

The higher crush forces, and hence enhanced crush absorbing properties, of the hybrids with [±45] off-centred BFRP plies can be explained by examining the failure mode analyses in Figs. 12–14. While the majority of the hybrid samples displayed extensive splaying due to debonding between wood veneers and BFRP plies, the adhesion between the dissimilar materials in two out of the four tested [±45] off-centred configurations shown in Fig. 14 remained intact, inhibiting the onset and evolution of splaying. It is known that splaying leads to reduced energy-absorbing capabilities [8]. The findings presented herein indicate that the positioning and orientation of BFRP plies within wood-BFRP hybrid materials may play a role in preventing or delaying splaying during axial crushing. Section 5.3 will discuss this further. The results certainly confirm that intact interfaces prevent splaying, leading to higher energy absorption. Table 6 shows that the two samples without debonding (③ and ④) of hybrids with [±45] off-centred BFRP plies yield SEA values of 40.54 kJ/kg and 38.35 kJ/kg, substantially higher values compared to all other SEA values measured from the same and other hybrid configurations. It should be noted that in these two cases, the hybrid wood-BFRP laminates achieved 82 %–86 % of the SEA measured from pure BFRP laminates by only using two layers of BFRP in combination with wood veneers.

5.2. Rule of mixture

The force vs displacement graphs obtained from the pure materials in Fig. 20(a) can be combined through the rule of mixture outlined in Equation (4). The proportion r in Equation (4) represents the ratio between the thickness of the BFRP plies and the total thickness of the hybrid samples. This ratio is considered to be $r = 0.25$ for all of the following calculations. An alternative approach would be to determine the proportion r based on the densities. A comparison between thickness-based and density-based values revealed negligible differences.

With respect to the force vs displacement graphs, the rule of mixtures is applied point-wise to the graphs obtained from the pure materials shown in Fig. 20(a). Fig. 21 compares the experimental mean of the hybrid samples (centred and off-centred configurations) with the theoretically calculated graphs. It can be seen that the rule of mixtures can accurately reproduce the response of the hybrid materials with [0/90] oriented BFRP laminates as shown in Fig. 21(a), as well as hybrids with centred [±45] BFRP plies, see Fig. 21(b). However, the rule of mixtures is not applicable to the hybrid materials with the off-centred [±45] BFRP plies, as demonstrated in Fig. 21(b).

A similar conclusion can be drawn from the evaluation of SEA values presented in Table 7. By considering the mean SEA values of the pure materials, the rule of mixture can estimate the mean SEA values obtained from hybrid samples with centred and off-centred [0/90] BFRP plies, as well as centred [±45] BFRP plies. The discrepancies between estimations and measured values for these cases are 1 %–12 %. The high mean SEA value of 33.18 kJ/kg measured from hybrids with off-centred [±45] BFRP plies cannot be predicted. Both estimations for crush efficiency are deemed reasonable, with values well within the measured range of mean values from centred and off-centred hybrid configurations.

The results indicate that the rule of mixture can estimate CE irrespective of the location and orientation of the BFRP plies, or the dominant failure mode. Furthermore, it can be applied to estimate SEA and force vs displacement graphs when significant splaying is observed. However, it cannot predict the overall crush behaviour when other failure modes are dominant. This can be explained by the fact that significant splaying leads to isolated material layers (here separated wood and BFRP laminates), which act independently of each other. Such independent behaviour enables the summation of the individual parts of the hybrid by means of rule of mixture, as observed for hybrid configurations with [0/90] BFRP plies (centred and off-centred), as well as with centred [±45] BFRP plies. However, to maximise energy-absorption, it is shown that splaying should be minimised. Since the rule of mixture is not applicable in these cases, more sophisticated analysis tools, such as finite element analysis [34,35], are required to exploit the full potential for the design

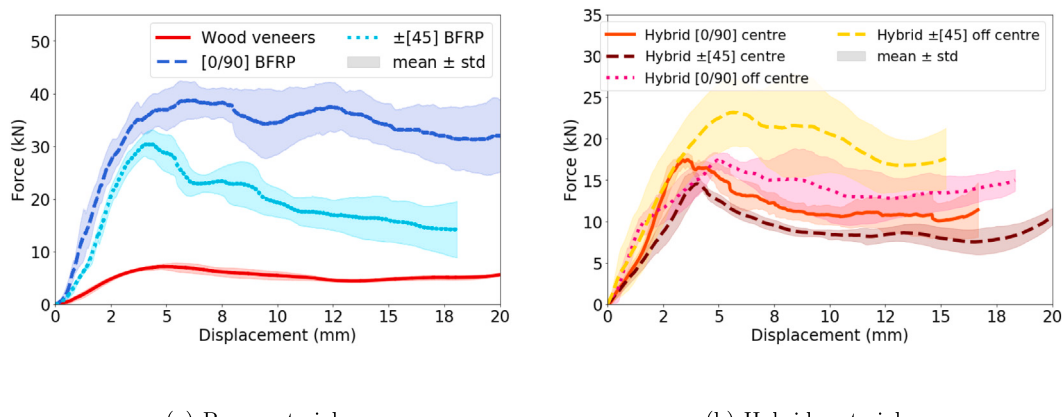


Fig. 20. Direct comparison of force vs displacement graphs between (a) pure wood and BFRP materials, and between (b) hybrid combinations varying location and orientation of BFRP plies.

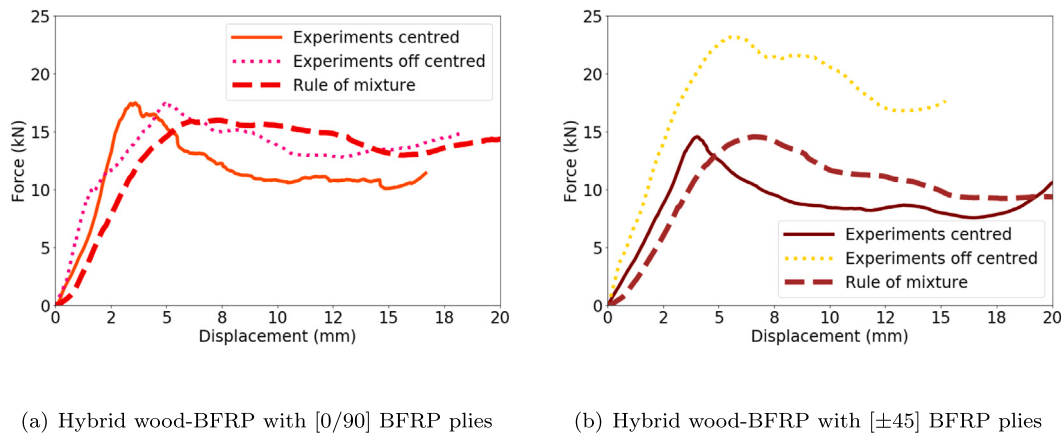


Fig. 21. Measured crush responses in centred and off-centred tests compared to estimated results from rule of mixture in Equation (4).

Table 7

Quantitative comparison of Specific Energy Absorption (SEA) and Crush Efficiency (CE) obtained from experiments of hybrid wood-BFRP laminates and rule of mixture in Equation (4).

SEA (kJ/kg)	Experiments Rule of mixture	Hybrids with [0/90] BFRP plies		Hybrids with [±45] BFRP plies	
		Centred	Off-centred	Centred	Off-centred
SEA (kJ/kg)	Experiments Rule of mixture	26.52 23.43	26.81	18.91 18.86	33.18
CE (-)	Experiments Rule of mixture	0.63 0.71	0.74	0.59 0.67	0.75

of hybrid wood-BFRP configurations. At best, the rule of mixture can provide (overly) conservative estimates of the crush behaviour in these cases.

5.3. Root cause analysis

Two important questions arising from the previously presented results are i) whether the layup and/or location of the BFRP plies can mechanistically explain the findings of the hybrid laminates, and ii) whether there are any manufacturing-related irregularities present.

Classical Laminate Theory

To address the first question, Classical Laminate Theory (CLT) was applied to investigate the stress distribution through the thickness of the various hybrid material configurations. Given the transversely isotropic material properties listed in Table 8, CLT evaluates the stiffness \mathbf{Q}_k in each ply k of the laminate, as determined by

$$\mathbf{Q}_k = \begin{bmatrix} Q_{11} & Q_{12} & 0 \\ Q_{21} & Q_{22} & 0 \\ 0 & 0 & Q_{66} \end{bmatrix} \quad (5)$$

with $Q_{11} = \frac{E_1}{1-v_{12}v_{21}}$, $Q_{12} = Q_{21} = \frac{v_{12}E_2}{1-v_{12}v_{21}}$, $Q_{22} = \frac{E_2}{1-v_{12}v_{21}}$ and $Q_{66} = G_{12}$.

The stiffness matrix is transformed into global coordinates by the rotation matrix \mathbf{T} such that $\bar{\mathbf{Q}}_k = \mathbf{T}^T \mathbf{Q}_k \mathbf{T}$. Accounting for the through-thickness position of each ply z_k and its thickness, ABD matrices are

given by

$$\begin{aligned} A_{ij} &= \sum_{k=1}^n \{\bar{\mathbf{Q}}_{ij}\}_n (z_k - z_{k-1}) \\ B_{ij} &= \frac{1}{2} \sum_{k=1}^n \{\bar{\mathbf{Q}}_{ij}\}_n (z_k^2 - z_{k-1}^2) \\ D_{ij} &= \frac{1}{3} \sum_{k=1}^n \{\bar{\mathbf{Q}}_{ij}\}_n (z_k^3 - z_{k-1}^3), \end{aligned} \quad (6)$$

where \mathbf{A} is the extension stiffness, \mathbf{B} the extension-bending coupling matrix, and \mathbf{D} the bending stiffness.

For globally applied normal forces $\mathbf{N} = (N_x, N_y, N_{xy})$ and moments $\mathbf{M} = (M_x, M_y, M_{xy})$, the midplane strains $\boldsymbol{\epsilon}^0 = (\epsilon_{xx}^0, \epsilon_{yy}^0, \epsilon_{xy}^0)$ and curvatures $\boldsymbol{\kappa} = (\kappa_{xx}, \kappa_{yy}, \kappa_{xy})$ can be calculated by

$$\begin{bmatrix} \boldsymbol{\epsilon}^0 \\ \boldsymbol{\kappa} \end{bmatrix} = \begin{bmatrix} \mathbf{A} & \mathbf{B} \\ \mathbf{B} & \mathbf{D} \end{bmatrix}^{-1} \begin{bmatrix} \mathbf{N} \\ \mathbf{M} \end{bmatrix}. \quad (7)$$

The ply strains in global coordinates $\boldsymbol{\epsilon} = (\epsilon_{xx}, \epsilon_{yy}, \epsilon_{xy})$ are obtained by

$$\boldsymbol{\epsilon} = \boldsymbol{\epsilon}^0 + \mathbf{z}\boldsymbol{\kappa}. \quad (8)$$

By transforming the global strain into the local coordinates of each ply k such that $\boldsymbol{\epsilon}_k = \mathbf{T}\boldsymbol{\epsilon}$, the ply stresses $\boldsymbol{\sigma}_k = \bar{\mathbf{Q}}_k \boldsymbol{\epsilon}_k$ can be evaluated. The local ply stresses $\boldsymbol{\sigma}_k = (\sigma_x, \sigma_y, \sigma_{xy})$ consist of the longitudinal σ_x , transverse σ_y and shear σ_{xy} stress components.

The through-thickness stress distributions of longitudinal ply stresses σ_x in the different hybrid material configurations are shown in Fig. 22. These results refer to a small axial force N_x applied in the global x -direction, which is aligned with the direction of axial crushing. All other forces and moments are set to zero. It should be noted that CLT can only provide a qualitative comparison of stresses among the hybrid layups within the elastic regime, as it does not account for material non-linearities and debonding. The results presented in Fig. 22 do not show

Table 8
Elastic properties of wood veneers and BFRP plies.

	E_1 (GPa)	E_2 (GPa)	G_{12} (GPa)	v_{12} (-)
Wood veneers [35]	14	2.28	1.08	0.073
BFRP [24]	11.54	11.54	2.4	0.3

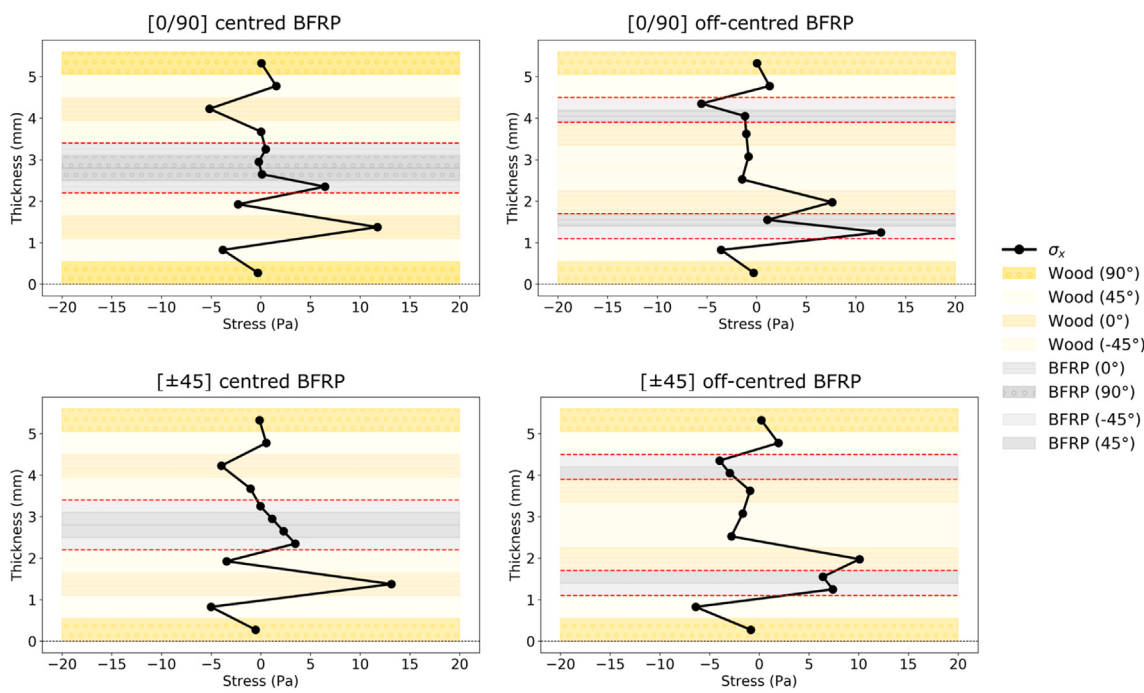


Fig. 22. Through-thickness axial stress analysis in various hybrid wood-BFRP material combinations applying classical laminate theory.

any clear tendencies towards higher stresses or significant stress jumps between BFRP and wood plies in a specific hybrid configuration. This suggests that the layup and location of the BFRP plies do not influence the mechanical (elastic) response.

Finite Element Simulation of Pressure Profile

Prior to conducting the debonding fracture tests and the axial crush tests, the thickness measurements listed in Tables 1 and 2 highlighted the influence of pressure and pressing time, as well as the irregularities along the cross-sections of the omega-shaped test specimens. The failure mode analysis in Section 4.2 demonstrated that the debonding locations in the hybrid configurations corresponded with the thicker regions of the cross-section measured in the curved regions of the omega shape.

A finite element analysis of the pressing process during manufacturing (see Fig. 5) was performed in the finite element software Abaqus/Explicit [36] to explain these findings. The top and bottom moulds were modelled as three-dimensional rigid bodies, along with the elastic wood test sample characterised by the properties listed in Table 8. As depicted in Fig. 23, a uniform displacement was applied to the top mould, while all degrees of freedom of the bottom mould were constrained. The resulting contact pressure shown in Fig. 23 provides an explanation for the inconsistent thickness measurements along the omega-shaped specimens. The non-uniform pressure profile reveals high contact pressure at the flat sections of the omega shape (t_1 , t_3 and t_5 in Fig. 4), and very low to no pressure in the curved regions (t_2 and t_4 in Fig. 4). With the knowledge of the high sensitivity of the wood-BFRP interfaces to pressure and pressing time observed in Section 3, the findings from Fig. 23, together with the thickness measurements prior to axial crush testing shown in Table 2, confirm that manufacturing-related challenges in producing non-flat geometries must be addressed to design and build highly energy-absorbing hybrid materials. Uniform pressure along the cross-section of the non-flat samples is essential to enhance bonding between wood and BFRP, thereby mitigating debonding during axial crushing and consequently leading to superior energy-absorbing capabilities of hybrid wood-BFRP materials.

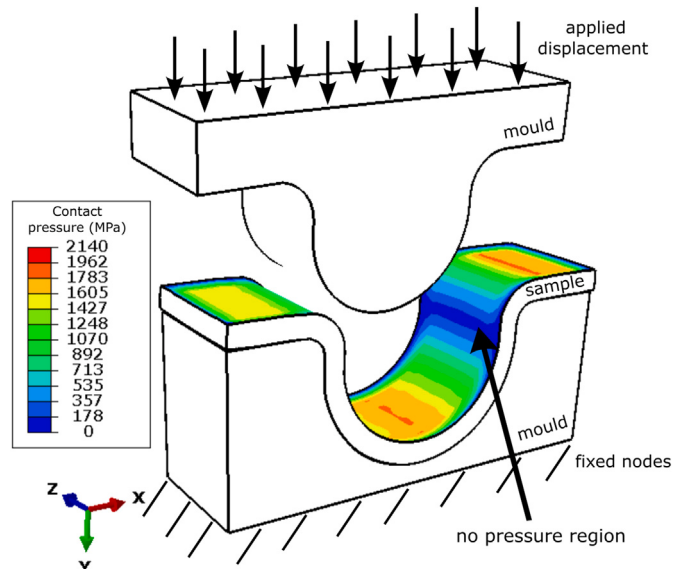


Fig. 23. Finite element analysis of the pressing process during the manufacturing of omega-shaped crush samples. No pressure regions highlight challenges in consistent manufacturing to avoid debonding during crushing.

5.4. Challenges & limitations

Hybrid materials with off-centred $\pm 45^\circ$ BFRP plies absorbed significantly more energy compared to the other hybrid configurations, primarily due to reduced splaying. This finding suggests that the interfacial bonding between the dissimilar materials plays a critical role in the design of energy-absorbing hybrid materials.

The root cause analysis in the previous section suggests that manufacturing-related factors are crucial for ensuring effective bonding

between wood and BFRP, whereas the layup and location of the BFRP plies are deemed less important according to CLT. It is important to note that the hybrid materials with off-centred [$\pm 45^\circ$] BFRP plies were manufactured last among all the hybrid samples. Although care was taken to fabricate the samples consistently, it is possible that the manufacturing process may have been inadvertently optimised, resulting in enhanced adhesion between the dissimilar materials. In addition, it is noteworthy that the debonding fracture tests presented in Section 2.2 investigated the bonding quality between [0/90] BFRP plies and [0] wood veneers. However, the BFRP plies and wood veneers were bonded at different angles in the investigated crush samples shown in Fig. 3. This relative orientation may also affect the wood-BFRP interface properties. Further research into efficient mould design is necessary to achieve more uniform pressure along the cross-section of the non-flat omega shape. Ultimately, high-fidelity analysis tools, such as analytical models [37] or finite element analysis [8,38], need to be developed to systematically examine the effects of BFRP layup and location within the hybrid configurations, considering material non-linearities and debonding. In addition to the simulation of typical failure modes in fibre-reinforced composites (fragmentation and splaying) [8], the consideration of densification observed in the wood veneer laminates during axial crushing further complicates these simulations.

With respect to crashworthiness, load cases other than axial crushing need to be considered to fully examine the energy-absorbing capabilities of the hybrid materials. Quasi-static and dynamic impact tests of pure wood veneers [31] should be extended to compare their performance to hybrid materials with varying orientation and location of the BFRP plies.

6. Conclusion

This study compared pure wood veneers and Basalt Fibre Reinforced Polymer (BFRP) laminates with hybrid combinations in quasi-static axial crush tests to investigate the design of sustainable hybrid materials and their energy absorption capabilities. The findings indicate that the insertion of thin BFRP plies into quasi-isotropic wood veneers enhances the energy absorption capacity during axial crushing, with enhanced Specific Energy Absorption (SEA) increasing from 15.25 kJ/kg in pure wood veneers to 33.18 kJ/kg in hybrid wood-BFRP laminates. Furthermore, the study demonstrated that debonding between the two dissimilar materials reduces energy absorption due to splaying. In these instances, a simple rule of mixtures can be applied to estimate the crush behaviour of hybrid laminates by considering only the crush responses from the two pure materials. Debonding fracture tests and simulations of the pressing process during manufacturing demonstrated that non-uniform pressure along the curved, omega-shaped test samples should be avoided to produce crashworthy hybrid wood-BFRP materials. To fully explore the potential of sustainable hybrid materials, more sophisticated analysis tools are necessary to confidently design energy-absorbing materials and structures for next-generation transport vehicles.

CRediT authorship contribution statement

Johannes Reiner: Writing – review & editing, Writing – original draft, Visualization, Validation, Supervision, Methodology, Investigation, Formal analysis, Data curation, Conceptualization. **Mahbube Subhani:** Writing – review & editing, Supervision, Methodology, Conceptualization. **Matt Jennings:** Writing – review & editing, Supervision, Investigation, Conceptualization.

Declaration of competing interest

The authors declare that they have no known competing financial interests or personal relationships that could have appeared to influence the work reported in this paper.

Acknowledgements

The authors would like to thank undergraduate students from Deakin University Darren Narain, Connor Anthian, James Gregg and Tahj Beardsley for their support in the manufacturing and mechanical testing of pure wood laminates and hybrid configurations. In addition, thanks to exchange student Chloe Crespino who manufactured and tested the pure BFRP laminates. The authors would like to acknowledge Henkel for providing Purbond HB S109.

Data availability

Data will be made available upon request.

References

- [1] Tsai W-T. Carbon-negative policies by reusing waste wood as material and energy resources for mitigating greenhouse gas emissions in Taiwan. *Atmosphere* 2021;12(9). <https://doi.org/10.3390/atmos12091220>. <https://www.mdpi.com/2073-4433/12/9/1220>
- [2] Li M, He M, Li Z, Yun X. Flexural behavior of lvl made from Australian radiata pine. *Structures* 2024;6:106014. <https://doi.org/10.1016/j.istruc.2024.106014>
- [3] Aura-Aero. Aura-aero. 2025. URL:<https://aura-aero.com/en/>
- [4] Mohammed I, Ansari MNM, Pua G, Jawaid M, Islam MS. A review on natural fiber reinforced polymer composite and its applications. *Int J Polym Sci* 2015;2015(1):243947. <https://doi.org/10.1155/2015/243947>
- [5] Mishra T, Mandal P, Rout AK, Sahoo D. A state-of-the-art review on potential applications of natural fiber-reinforced polymer composite filled with inorganic nanoparticle. *Composites Part C: Open Access* 2022;9:100298. <https://doi.org/10.1016/j.jcomc.2022.100298>. <https://www.sciencedirect.com/science/article/pii/S2666682022000627>
- [6] Elfaleh I, Abbassi F, Habibi M, Ahmad F, Guedri M, Nasri M, et al. A comprehensive review of natural fibers and their composites: an eco-friendly alternative to conventional materials. *Results Eng* 2023;19:101271. <https://doi.org/10.1016/j.rineng.2023.101271>. <https://www.sciencedirect.com/science/article/pii/S2590123023003985>
- [7] Abramowicz W. Thin-walled structures as impact energy absorbers. *Thin-Walled Struct* 2003;41(2):91–107, buckling strength and Failure Mechanics of Thin walled structures. [https://doi.org/10.1016/S0263-8231\(02\)00082-4](https://doi.org/10.1016/S0263-8231(02)00082-4). <https://www.sciencedirect.com/science/article/pii/S0263823102000824>
- [8] Reiner J, Feser T, Waime M, Poursartip A, Voggenreiter H, Vaziri R. Axial crush simulation of composites using continuum damage mechanics: Fe software and material model independent considerations. *Composites Part B: Engineering* 2021;225:109284. <https://doi.org/10.1016/j.compositesb.2021.109284>. <https://www.sciencedirect.com/science/article/pii/S1359836821006594>
- [9] Ataabadi P, Karagiozova D, Alves M. Crushing and energy absorption mechanisms of carbon fiber-epoxy tubes under axial impact. *Int J Impact Eng* 2019;131:174–89. <https://doi.org/10.1016/j.ijimpeng.2019.03.006>. <https://www.sciencedirect.com/science/article/pii/S0734743X18312090>
- [10] Ha NS, Lu G. A review of recent research on bio-inspired structures and materials for energy absorption applications, composites Part B: Engineering 2020;181:107496. <https://doi.org/10.1016/j.compositesb.2019.107496>. <https://www.sciencedirect.com/science/article/pii/S1359836819339964>
- [11] Zhang Y, Wang J, Lin J, Zhang F, Yan X. Crushing Mechanical responses of natural wood columns and wood-filled composite columns. *Eng Fail Anal* 2021;124:105358. <https://doi.org/10.1016/j.engfailanal.2021.105358>
- [12] Guélou R, Eyma F, Cantarel A, et al., A comparison of three wood species (poplar, birch and oak) for crash application. *Eur J Wood Prod* 2023;81:125–41. <https://doi.org/10.1007/s00107-022-01871-x>
- [13] Guélou R, Eyma F, Cantarel A, Rivallant S, Castanié B. Crashworthiness of poplar wood veneer tubes. *Int J Impact Eng* 2021;147:103738. <https://doi.org/10.1016/j.ijimpeng.2020.103738>. <https://www.sciencedirect.com/science/article/pii/S0734743X20308083>
- [14] Guélou R, Eyma F, Cantarel A, Rivallant S, Castanié B. Static crushing of wood based sandwich composite tubes. *Compos Struct* 2021;273:114317. <https://doi.org/10.1016/j.compstruct.2021.114317>. <https://www.sciencedirect.com/science/article/pii/S0263822321007790>
- [15] Yan L, Chouw N, Jayaraman K. On energy absorption capacity, flexural and dynamic properties of flax/epoxy composite tubes. *Fiber And Polym* 2014;15:1270–77. <https://api.semanticscholar.org/CorpusID:135777090>
- [16] Yan L, Chouw N. Crashworthiness characteristics of flax fibre reinforced epoxy tubes for energy absorption application. *Materials & Design* 2013;51:629–40. <https://doi.org/10.1016/j.matdes.2013.04.014>. <https://www.sciencedirect.com/science/article/pii/S0261306913003294>
- [17] Attia MA, El-Baky MAA, Hassan MA, Sebaey TA, Mahdi E. Crashworthiness characteristics of carbon-jute-glass reinforced epoxy composite circular tubes. *Polym Compos* 2018;39(S4):E2245–61. <https://doi.org/10.1002/pc.24597>. <https://4sepublications.onlinelibrary.wiley.com/doi/abs/10.1002/pc.24597>
- [18] Sivagurunathan R, Lau Tze Way S, Sivagurunathan L, et al. The effects of triggering mechanisms on the energy absorption capability of circular jute/epoxy composite tubes under quasi-static axial loading. *Appl Compos Mater* 2018;25:1401–17. <https://doi.org/10.1007/s10443-018-9673-5>

- [19] Ismail AE. Energy absorption performance of conical natural fiber reinforced composites. 2006). URL:https://www.academia.edu/3012764/Energy_absorption_performance_of_conical_natural_fiber_reinforced_composites_Abstract
- [20] Yang H, Lei H, Lu G, Zhang Z, Li X, Liu Y. Energy absorption and failure pattern of hybrid composite tubes under quasi-static axial compression, composites Part B: Engineering 2020;198:108217. <https://doi.org/10.1016/j.compositesb.2020.108217>. <https://www.sciencedirect.com/science/article/pii/S1359836820332674>
- [21] Supian A, Sapuan S, Zuhri M, Zainudin E, Ya H. Crashworthiness performance of hybrid kenaf/glass fiber reinforced epoxy tube on winding orientation effect under quasi-static compression load. Def Technol 2020;16(5):1051–61. <https://doi.org/10.1016/j.dt.2019.11.012>. <https://www.sciencedirect.com/science/article/pii/S2214914719307469>
- [22] Khalid AA, Sahari B, Khalid Y. Performance of composite cones under axial compression loading. Compos Sci Technol 2002;62(1):17–27. [https://doi.org/10.1016/S0266-3538\(01\)00092-6](https://doi.org/10.1016/S0266-3538(01)00092-6). <https://www.sciencedirect.com/science/article/pii/S0266353801000926>
- [23] Stapleton SE, Adams DO. Crush initiators for increased energy absorption in composite sandwich structures. J Sandw Struct Mater 2008;10(4):331–54. <https://doi.org/10.1177/1099636208091737>
- [24] Don DK, Reiner J, Jennings M, Subhani M. Basalt fibre-reinforced polymer laminates with eco-friendly bio resin: a comparative study of Mechanical and fracture properties. Polymers 2024;16(14). <https://doi.org/10.3390/polym16142056>. <https://www.mdpi.com/2073-4360/16/14/2056>
- [25] Heyner D, Piazza G, Beeh E, Seidel G, Friedrich H, Kohl D, et al. Innovative concepts for the usage of veneer-based hybrid materials in vehicle structures, proceedings of the institution of mechanical engineers. Part L: Journal Of Materials: Design And Applications 2021;235(6):1302–11. <https://doi.org/10.1177/1464420721998398>
- [26] Li H, Zhou W, Jian B, Shen X, Lorenzo R, Ashraf M. Experimental evaluation on the axial crushing performance of bfrp bamboo winding composite hollow components; 2024 9.
- [27] Fernando D, Frangi A, Kobel P. Behaviour of basalt fibre reinforced polymer strengthened timber laminates under tensile loading. Eng Struct 2016;117:437–56. <https://doi.org/10.1016/j.engstruct.2016.03.009>
- [28] Thorhallsson ER, Hinriksson GI, Snabjornsson JT. Strength and stiffness of glulam beams reinforced with glass and basalt fibres, composites Part B: Engineering 2017;115:300–07, composite lattices and multiscale innovative materials and structures. <https://doi.org/10.1016/j.compositesb.2016.09.074>
- [29] Orellana S, Hadi K, Narain D, Jennings M, Subhani M, Reiner J. Effects of manufacturing parameters on Mechanical interface properties of thin wood veneer laminates. Int J Adhes Adhes 2024;130:103614. <https://doi.org/10.1016/j.ijadhadh.2023.103614>. <https://www.sciencedirect.com/science/article/pii/S0143749623002944>
- [30] Reiner J, Pizarro SO, Hadi K, Narain D, Zhang P, Jennings M, et al. Damage resistance and open-hole strength of thin veneer laminates: adopting design and testing principles from fibre-reinforced polymers. Eng Fail Anal 2023;143:106880. <https://doi.org/10.1016/j.englfailanal.2022.106880>. <https://www.sciencedirect.com/science/article/pii/S1350630722008470>
- [31] Reiner J, Irshad YG, Orellana S, Feser T, Waimer M, Jennings M, et al. Experimental investigation of quasi-static and dynamic impact resistance in thin wood veneer laminates. Forests 2024;15(4). <https://doi.org/10.3390/f15040694>. <https://www.mdpi.com/1999-4907/15/4/694>
- [32] Neale G, Dahale M, Yoo S, Toso N, McGarrigle C, Quinn J, et al. Improved crush energy absorption in 3d woven composites by pick density modification. Composites Part B: Engineering 2020;192:108007. <https://doi.org/10.1016/j.compositesb.2020.108007>. <https://www.sciencedirect.com/science/article/pii/S1359836819348966>
- [33] Ramakrishna S. Microstructural design of composite materials for crash-worthy structural applications. Materials & Design 1997;18(3):167–73. [https://doi.org/10.1016/S0261-3069\(97\)00098-8](https://doi.org/10.1016/S0261-3069(97)00098-8). <https://www.sciencedirect.com/science/article/pii/S0261306997000988>
- [34] Reiner J, Fu Y-F. Data-driven parameter identification to simulate progressive damage in fiber reinforced laminates under low velocity impact. Int J Impact Eng 2023;180:104711. <https://doi.org/10.1016/j.ijimpeng.2023.104711>. <https://www.sciencedirect.com/science/article/pii/S0734743X23002221>
- [35] Reiner J, Fu Y-F, Feser T. Progressive damage simulation of wood veneer laminates and their uncertainty using finite element analysis informed by genetic algorithms. Applied Sciences 2024;14(11). <https://doi.org/10.3390/app14114511>. <https://www.mdpi.com/2076-3417/14/11/4511>
- [36] Smith M. ABAQUS/Standard User's manual, version 6.9. United States: Dassault Systèmes Simulia Corp; 2009.
- [37] Hussein RD, Ruan D, Lu G. An analytical model of square cfrp tubes subjected to axial compression. Compos Sci Technol 2018;168:170–78. <https://doi.org/10.1016/j.compscitech.2018.09.019>. <https://www.sciencedirect.com/science/article/pii/S0266353818306900>
- [38] Li M, Zhao J, Wang G. Extended finite element analysis on size effects of bending performance for Chinese larch pine laminated veneer lumber. Structures 2025;74:108510. <https://doi.org/10.1016/j.istruc.2025.108510>